Anisotropic terahertz response from a strong-field ionized electron-ion plasma

B. Pasenow,[1,2] C. Dineen,[1,2] J. Hader,[2,3] M. Brio,[1] J. V. Moloney,[1,2,*] S. W. Koch,[2,4] S. H. Chen,[5,†]
A. Becker,[5] and A. Jaroń-Becker[5]

[1]*Arizona Center for Mathematical Sciences, Department of Mathematics, University of Arizona, Tucson, Arizona 85721, USA*
[2]*College of Optical Sciences, University of Arizona, Tucson, Arizona 85721, USA*
[3]*Nonlinear Control Strategies Inc., Tucson, Arizona 85705, USA*
[4]*Department of Physics and Material Sciences Center, Philipps-University, 35032 Marburg, Germany*
[5]*JILA and Department of Physics, University of Colorado at Boulder, Boulder, Colorado 80309-0440, USA*

A microscopic theory is adapted to compute the time-resolved terahertz (THz) probe response of a dynamically evolving, strong-field ionized electron-ion plasma. The numerical solutions show that the relaxation of the initially highly anisotropic carrier distributions leads to a polarization dependent short-time THz response. This THz polarization discrimination gradually vanishes as the plasma approaches a thermodynamic equilibrium configuration via electron-electron and electron-ion scattering. The detailed carrier-relaxation dynamics causes a strongly nonmonotonic time-development of the THz absorption.

I. INTRODUCTION

Ultrashort pulse (USP) photoionization plays an important role in high harmonic generation (HHG) and in filamentation associated with extended propagation in air. Filamentation in high-pressure gas-filled capillaries has recently been reported as the mechanism for generating coherent x-ray pulsed beams via generation of the 5000th harmonic of a 3.9-μ fundamental [1]. Recent femtosecond resolved measurements of the ionized photoelectron angular distributions using velocity map imaging have raised fundamental questions regarding the state of the plasma generated by the USP [2]. Full 3D quantum Schrödinger equation simulations of an atom in a strong few-cycle laser pulse confirm these experimental observations [3]. The latter are based on single-electron quantum calculations and do not account for mutual scattering of the freed electrons and ions mediated by the Coulomb potential.

In our previous investigations [4], we presented a microscopic analysis of the short-time dynamics of photoionized electrons created by an intense few-cycle laser pulse. After the USP, the photoionized free electrons are left in a highly anisotropic, nonequilibrium momentum distribution. On a timescale, longer than the ionizing pulse, Coulomb scattering of electrons and ions equilibrates the distribution toward an electron plasma state with an isotropic Fermi-Dirac momentum distribution.

To experimentally observe the transition from nonequilibrium ionized electron distributions toward a state with isotropic Fermi-Dirac distributions, one needs a probe that is sensitive to the internal transitions of the system. For the typical parameters in strong-field ionization studies, the plasma frequency corresponds to excitations in the THz range of the electromagnetic spectrum. Hence, we suggest optical pump-THz probe experiments conceptually similar to those

done in semiconductors, where Huber *et al.* showed "how many-particle interactions develop after ultrafast excitation of an electron-hole plasma" [5].

In this paper, we follow the Ansatz used by Golde *et al.* [6] who calculated the THz response of a two-dimensional (static) electron gas. By expanding the Coulomb-interacting many-electron-ion Hamiltonian by the relevant light-matter interaction contributions, our theory is capable of describing the interaction of a THz probe field with our dynamical electron distributions. Calculating the linear THz current, we show that within an inverse plasma frequency the optical response reflects the anisotropy of the system.

In the following sections we present our theoretical model (Sec. II), expand the relevant equations up to the linear THz response (Sec. III), show and discuss some representative numerical results (Sec. IV), and finish with a short summary (Sec. V). In the Appendix we give further information on our Monte Carlo implementation of the Coulomb scattering dynamics on a general purpose graphics processing unit (GPGPU), which gives a significant speedup in comparison to a single CPU implementation.

II. THEORETICAL MODEL

In this paper, we treat the situation where an ultrashort strong laser pulse ionizes a hydrogen atom. Assuming a random homogeneous distribution of ionized atoms, we use the resulting electron-ion state as initial condition for the subsequent carrier dynamics. The ionization process is described by solving the time-dependent Schrödinger equation (TDSE). For the electron quantum kinetics, we use the Heisenberg equation-of-motion approach evaluating the commutator between the relevant Hamiltonian and the operator of interest $-i\hbar \frac{d}{dt} A = [H, A]_-$. The Hamiltonian includes the free-particle kinetic energy of the electrons and ions

$$H_{\text{kin}}^\lambda = \sum_{\lambda,\mathbf{k}} E_{\mathbf{k}}^\lambda a_{\lambda\mathbf{k}}^+ a_{\lambda\mathbf{k}}, \quad \text{with } E_{\mathbf{k}}^\lambda = \frac{\hbar^2 k^2}{2m_\lambda}. \quad (1)$$

*jml@acms.arizona.edu
†Present Address: Department of Physics and Astronomy, Louisiana State University, Baton Rouge, Louisiana 70803, USA.

The interaction with a classical THz field is described in the $\mathbf{A} \cdot \mathbf{p}$ picture (velocity gauge)

$$H_{\mathbf{A} \cdot \mathbf{p}} \simeq -\sum_{\lambda, \mathbf{k}} \mathbf{J}_{\lambda \mathbf{k}}^{\text{THz}} \cdot \mathbf{A} a_{\lambda \mathbf{k}}^+ a_{\lambda \mathbf{k}}$$

$$H_{\mathbf{A} \cdot \mathbf{A}} \simeq -\sum_{\lambda, \mathbf{k}} \tfrac{1}{2} \mathbf{J}_{\lambda}^{\text{pond}} \cdot \mathbf{A} a_{\lambda \mathbf{k}}^+ a_{\lambda \mathbf{k}} \qquad (2)$$

with $\mathbf{J}_{\lambda \mathbf{k}}^{\text{THz}} = \frac{q_\lambda}{m_\lambda} \hbar \mathbf{k}$ and $\mathbf{J}_{\lambda}^{\text{pond}} = -\frac{q_\lambda}{m_\lambda} q_\lambda \mathbf{A}$,

which is connected to the $\mathbf{E} \cdot r$ picture (length gauge) by an unitary transformation (the Göppert-Mayer Transformation [7]). The Coulomb-interaction part of the Hamiltonian is

$$H_C = \frac{1}{2} \sum_{\lambda, \rho, \mathbf{k}, \mathbf{p}, \mathbf{q}} V_{|\mathbf{q}|}^{\lambda \rho} a_{\lambda \mathbf{k}}^+ a_{\rho \mathbf{p}}^+ a_{\rho \mathbf{p} + \mathbf{q}} a_{\lambda \mathbf{k} - \mathbf{q}},$$

$$\text{with } L^3 V_{|\mathbf{q}|}^{\lambda \rho} = \frac{q_e^2}{\epsilon_0 [q^2 + \kappa_D^2]}. \qquad (3)$$

Here, the operator $a_{\lambda \mathbf{k}}^+$ ($a_{\lambda \mathbf{k}}$) creates (destroys) an electron ($\lambda = e$) or ion ($\lambda = i$) with momentum $\mathbf{k}$. Sums over the particle type $\lambda \in \{e, i\}$ always include the two-fold spin degeneracy. The momentum sums are treated in the limit $\frac{1}{L^3} \sum_{\mathbf{k}} [\ldots] \rightarrow \frac{1}{(2\pi)^3} \int [\ldots] d^3 k$ when the equations are solved numerically. The Coulomb matrix element is screened by the inverse Debye screening length $\kappa_D = \sqrt{\frac{q_e^2 N_e^{\text{tot}}}{\epsilon_0 k_B T_e}}$ [8].

In the velocity gauge, the pondermotive current $\mathbf{J}_{\lambda}^{\text{pond}}$ is analytically separated from the other THz current contributions $\mathbf{J}_{\lambda}^{\text{THz}}$. For the electrons, we obtain

$$\mathbf{J}_e = \frac{1}{L^3} \sum_{e, \mathbf{k}} \left[\mathbf{J}_{e\mathbf{k}}^{\text{THz}} + \mathbf{J}_e^{\text{pond}} \right] f_{e\mathbf{k}}$$

$$= \left[\frac{1}{L^3} \sum_{\mathbf{k}} \frac{q_e}{m_e} \hbar \mathbf{k} \, f_{e\mathbf{k}} - \epsilon_0 (\omega_{\text{pl}}^e)^2 \mathbf{A} \right] \qquad (4)$$

with $\omega_{\text{pl}}^e = \sqrt{\frac{q_e^2 N_e^{\text{tot}}}{\epsilon_0 m_e}}$, $N_e^{\text{tot}} = \sum_e N_e = \frac{2}{L^3} \sum_{\mathbf{k}} f_{e\mathbf{k}}$.

Here, the pondermotive part results from the $H_{\mathbf{A} \cdot \mathbf{A}}$ Hamiltonian, whereas the THz current is due to the $H_{\mathbf{A} \cdot \mathbf{p}}$ part. For the ions, we obtain an equation similar to Eq. (4) with the main difference that here the ion mass and ion charge enters. Due to the large mass difference $m_i > 1800 \, m_e$, the ion contributions to the current can be neglected allowing us to restrict the treatment to the electron density $f_{e\mathbf{k}} = \langle a_{e\mathbf{k}}^+ a_{e\mathbf{k}} \rangle$,

$$\hbar \partial_t f_{e\mathbf{k}} = 2 \sum_{\rho, \mathbf{p}} \sum_{\mathbf{q} \neq \mathbf{0}} V_{|\mathbf{q}|}^{e\rho} \text{Im}[\langle a_{e\mathbf{k}}^+ a_{\rho \mathbf{p}}^+ a_{\rho \mathbf{p} + \mathbf{q}} a_{e\mathbf{k} - \mathbf{q}} \rangle], \qquad (5)$$

with $\rho \in \{e, i\}$. We ignore the influence of the complex electron-ion polarization $p_{i\mathbf{k}}^e = \langle a_{e\mathbf{k}}^+ a_{i\mathbf{k}} \rangle$ induced by the optical (ionizing) field since we focus on times well after this field has decayed. The Coulomb part in the equation of motion shows the typical many-body hierarchy problem, i.e., the coupling of N-particle quantities to $(N + 1)$-particle quantities, which has to be systematically truncated at a specified level of correlations [9].

The two-particle correlation $\langle a_{\lambda \mathbf{k}}^+ a_{\rho \mathbf{p}}^+ a_{\rho \mathbf{p} + \mathbf{q}} a_{\lambda \mathbf{k} - \mathbf{q}} \rangle$ for $\mathbf{q} \neq 0$, e.g., consists of single-particle contributions $-\langle a_{\lambda \mathbf{k}}^+ a_{\rho \mathbf{p} + \mathbf{q}} \rangle \langle a_{\rho \mathbf{p}}^+ a_{\lambda \mathbf{k} - \mathbf{q}} \rangle$ and true two-particle correlations $\Delta \langle a_{\lambda \mathbf{k}}^+ a_{\rho \mathbf{p}}^+ a_{\rho \mathbf{p} + \mathbf{q}} a_{\lambda \mathbf{k} - \mathbf{q}} \rangle$. Since the electron-density dynamics couples to true electron-electron and electron-ion correlations, we additionally need the equations of motion

$$-i\hbar \partial_t \Delta \langle a_{e\mathbf{k}}^+ a_{\rho \mathbf{p}}^+ a_{\rho \mathbf{p} + \mathbf{q}} a_{e\mathbf{k} - \mathbf{q}} \rangle$$
$$= \left[\mathrm{E}_{\mathbf{k}}^e + \mathrm{E}_{\mathbf{p}}^\rho - \mathrm{E}_{\mathbf{p} + \mathbf{q}}^\rho - \mathrm{E}_{\mathbf{k} - \mathbf{q}}^e + i\eta \right] \Delta \langle a_{e\mathbf{k}}^+ a_{\rho \mathbf{p}}^+ a_{\rho \mathbf{p} + \mathbf{q}} a_{e\mathbf{k} - \mathbf{q}} \rangle$$
$$- \left[\mathbf{J}_{e\mathbf{q}}^{\text{THz}} - \mathbf{J}_{\rho \mathbf{q}}^{\text{THz}} \right] \cdot \mathbf{A}(t) \Delta \langle a_{e\mathbf{k}}^+ a_{\rho \mathbf{p}}^+ a_{\rho \mathbf{p} + \mathbf{q}} a_{e\mathbf{k} - \mathbf{q}} \rangle$$
$$+ \left[V_{|\mathbf{q}|}^{e\rho} - V_{|\mathbf{k} - \mathbf{p} - \mathbf{q}|}^{e\rho} \delta_\rho^e \right] [(1 - f_{e\mathbf{k}})(1 - f_{\rho \mathbf{p}}) f_{e\mathbf{k} - \mathbf{q}} f_{\rho \mathbf{p} + \mathbf{q}}]$$
$$- \left[V_{|\mathbf{q}|}^{e\rho} - V_{|\mathbf{k} - \mathbf{p} - \mathbf{q}|}^{e\rho} \delta_\rho^e \right] [f_{e\mathbf{k}} f_{\rho \mathbf{p}} (1 - f_{e\mathbf{k} - \mathbf{q}})(1 - f_{\rho \mathbf{p} + \mathbf{q}})]. \qquad (6)$$

Here, we kept only the lowest-order factorizations and neglected the coupling to other two-particle and higher-order correlations whose main contribution is approximated by introducing the dephasing η [9]. The last two lines of Eq. (6) show the typical Coulomb scattering into and out of the momentum state $(e, \mathbf{k})$. Assuming slowly varying densities, no electric field $\mathbf{A} = 0$, applying the Markov approximation to Eq. (6) and inserting the result in Eq. (5) gives the Boltzmann Coulomb scattering dynamics of free electrons:

$$\partial_t f_{e\mathbf{k}}|_{e-\lambda \text{ collision}}$$
$$= \frac{2\pi}{\hbar} \sum_{\mathbf{p}, \mathbf{q}} V_{|\mathbf{q}|}^2 (1 - f_{e\mathbf{k}})(1 - f_{\lambda \mathbf{p}}) f_{e\mathbf{k} - \mathbf{q}} f_{\lambda \mathbf{p} + \mathbf{q}} \delta (\Delta E_{\mathbf{k}, \mathbf{p}, \mathbf{q}}^{e, \lambda})$$
$$- \frac{2\pi}{\hbar} \sum_{\mathbf{p}, \mathbf{q}} V_{|\mathbf{q}|}^2 f_{e\mathbf{k}} f_{\lambda \mathbf{p}} (1 - f_{e\mathbf{k} - \mathbf{q}})(1 - f_{\lambda \mathbf{p} + \mathbf{q}}) \delta (\Delta E_{\mathbf{k}, \mathbf{p}, \mathbf{q}}^{e, \lambda})$$

with $\Delta E_{\mathbf{k}, \mathbf{p}, \mathbf{q}}^{e, \lambda} = \frac{\hbar^2 |\mathbf{k}|^2 - \hbar^2 |\mathbf{k} - \mathbf{q}|^2}{2 m_e} + \frac{\hbar^2 |\mathbf{p}|^2 - \hbar^2 |\mathbf{p} + \mathbf{q}|^2}{2 m_\lambda}$, $\qquad (7)$

where $\lambda \in \{e, i\}$. The δ distribution appears as the limit $\pi \delta(x) = \lim_{\eta \rightarrow 0} Im[-1/(x + i\eta)]$ of the imaginary part of the Markov energy denominator for small broadening η. This equation can be used for studying the relaxation dynamics from a nonequilibrium, anisotropic electron momentum distribution into an isotropic equilibrium plasma. A detailed description can be found in Ref. [4].

To compute the THz probe response of the dynamically changing electron distributions, we have to solve the electron-ion correlation Eq. (6) together with the equation for the electron density, Eq. (5). The detailed correlation dynamics Eq. (6) can be simplified by taking advantage of the fact that we are dealing with a dilute gas configuration. Due to the large mass difference, the ion energies can be neglected in comparison to electronic energies, i.e., $\mathrm{E}_{\mathbf{k}}^e + \mathrm{E}_{\mathbf{p}}^i - \mathrm{E}_{\mathbf{p} + \mathbf{q}}^i - \mathrm{E}_{\mathbf{k} - \mathbf{q}}^e \simeq \mathrm{E}_{\mathbf{k}}^e - \mathrm{E}_{\mathbf{k} - \mathbf{q}}^e$. For the same reasons, the ion current-matrix element $\mathbf{J}_{i\mathbf{k} - \mathbf{q}}^{\text{THz}}$ can be neglected in comparison to the electron current-matrix element $\mathbf{J}_{e\mathbf{k} - \mathbf{q}}^{\text{THz}}$. Furthermore, the ionic momentum-state occupation probabilities are way smaller than unity. Therefore, we can use $(1 - f_{i\mathbf{k}}) \simeq 1$ and $\sum_{\mathbf{p}} (1 - f_{i\mathbf{p}}) f_{i\mathbf{p} + \mathbf{q}} = \sum_{\mathbf{p}} (1 - f_{i\mathbf{p} + \mathbf{q}}) f_{i\mathbf{p}} \simeq L^3 N_i$. Defining the reduced

electron-ion correlation,

$$C_{\mathbf{k},\mathbf{k}-\mathbf{q}}^{ei} = \sum_{\mathbf{p}} \Delta \langle a_{e\mathbf{k}}^+ a_{i\mathbf{p}}^+ a_{i\mathbf{p}+\mathbf{q}} a_{e\mathbf{k}-\mathbf{q}} \rangle, \tag{8}$$

Eq. (6) transforms into

$$-i\hbar \partial_t C_{\mathbf{k},\mathbf{q}}^{ei}$$
$$= \left[E_{\mathbf{k}}^e - E_{\mathbf{q}}^e - \left(\mathbf{J}_{e\mathbf{k}-\mathbf{q}}^{\mathrm{THz}} - \mathbf{J}_{i\mathbf{k}-\mathbf{q}}^{\mathrm{THz}} \right) \cdot \mathbf{A}(t) + i\eta \right] C_{\mathbf{k},\mathbf{q}}^{ei}$$
$$- V_{|\mathbf{k}-\mathbf{q}|}^{ei} [f_{e\mathbf{k}} - f_{e\mathbf{q}}] L^3 N_i, \tag{9}$$

where the ions enter only via the integrated ion density $N_i = \frac{1}{L^3} \sum_{\mathbf{k}} f_{i\mathbf{k}}$. This equation, together with the density equation of motion,

$$\hbar \partial_t f_{e\mathbf{k}} = 2 \sum_{i,\mathbf{q} \neq \mathbf{k}} \mathrm{Im} \left[V_{|\mathbf{k}-\mathbf{q}|}^{ei} C_{\mathbf{k},\mathbf{q}}^{ei} \right] + \hbar \partial_t f_{e\mathbf{k}}|_{e-e\,\mathrm{collision}}, \tag{10}$$

describe the THz probe response of the electron momentum distributions.

III. THZ PROBE FIELD EXPANSION

Depending on the carrier envelope phase, the electron momentum distributions created by ultrashort few-cycle pulse ionization often show an asymmetry along the polarization direction of the light field. Therefore, the average momentum of these distributions is nonvanishing and leads to a finite electron current even without the THz probe field. A very effective procedure for separating these current contributions is to expand the equations in the order of the THz field $\mathbf{A}$. Since we are interested only in the linear THz probe response of the electron-ion system, we only need the zeroth- and first-order contributions. In zeroth order, i.e., without the probe field, we have to solve the Boltzmann collision dynamics Eq. (7). The resulting time-dependent distributions—labeled

here explicitly as $f_{e\mathbf{k}}^{(0)}$—are used as input for the first-order density equationw

$$\hbar \partial_t f_{e\mathbf{k}}^{(1)} = 2 \sum_{\mathbf{q}} V_{|\mathbf{k}-\mathbf{q}|}^{ei} \mathrm{Im} C_{\mathbf{k},\mathbf{q}}^{ei(1)} - \Gamma f_{e\mathbf{k}}^{(1)}, \tag{11}$$

where the true scattering contributions are treated using the relaxation time approximation

$$\partial_t f_{e\mathbf{k}}|_{e-e\,\mathrm{collision}} \simeq i\Gamma \left[f_{e\mathbf{k}}^{(\mathrm{FD})} - f_{e\mathbf{k}} \right].$$

Here, $f_{e\mathbf{k}}^{(\mathrm{FD})}$ is the final Fermi-Dirac distribution. The coupling to the THz field is governed by the first-order electron-ion correlation through

$$\left[-i\hbar \partial_t - \left(E_{\mathbf{k}}^e - E_{\mathbf{q}}^e + i\eta \right) \right] L^3 V_{|\mathbf{k}-\mathbf{q}|}^{ei} C_{\mathbf{k},\mathbf{q}}^{ei(1)}$$
$$= N_i^{\mathrm{tot}} \left(L^3 V_{|\mathbf{k}-\mathbf{q}|}^{ei} \right)^2 \left(f_{e\mathbf{q}}^{(1)} - f_{e\mathbf{k}}^{(1)} \right)$$
$$- \mathbf{J}_{e\mathbf{k}-\mathbf{q}}^{\mathrm{THz}} \cdot \mathbf{A}(t) \, L^3 V_{|\mathbf{k}-\mathbf{q}|}^{ei} C_{\mathbf{k},\mathbf{q}}^{ei(0)}. \tag{12}$$

For the solution of this equation we explicitly need the dynamics of the zeroth-order electron-ion correlation,

$$\left[-i\hbar \partial_t - \left(E_{\mathbf{k}}^e - E_{\mathbf{q}}^e + i\eta \right) \right] V_{|\mathbf{k}-\mathbf{q}|}^{ei} C_{\mathbf{k},\mathbf{q}}^{ei(0)}$$
$$= \left(V_{|\mathbf{k}-\mathbf{q}|}^{ei} \right)^2 \left(f_{e\mathbf{q}}^{(0)} - f_{e\mathbf{k}}^{(0)} \right) L^3 N_i^{\mathrm{tot}}, \tag{13}$$

which we solve in Markov approximation

$$L^3 V_{|\mathbf{k}-\mathbf{q}|}^{ei} C_{\mathbf{k},\mathbf{q}}^{ei(0)} \simeq N_i^{\mathrm{tot}} \left(L^3 V_{|\mathbf{k}-\mathbf{q}|}^{ei} \right)^2 \frac{f_{e\mathbf{k}}^{(0)} - f_{e\mathbf{q}}^{(0)}}{E_{\mathbf{k}}^e - E_{\mathbf{q}}^e + i\eta}. \tag{14}$$

For the further treatment, we Fourier transform the first-order equation

$$f(\omega) := F_\omega[f(t)] = \int_{-\infty}^{\infty} e^{-i\omega t} f(t) dt. \tag{15}$$

Inserting the correlation contributions into Eq. (11) yields

$$(\hbar\omega + i\Gamma) f_{e\mathbf{k}}^{(1)}(\omega) = \frac{1}{L^3} \sum_{\mathbf{q}} N_i^{\mathrm{tot}} \left(L^3 V_{|\mathbf{k}-\mathbf{q}|}^{ei} \right)^2 \left\{ \frac{f_{e\mathbf{k}}^{(1)}(\omega) - f_{e\mathbf{q}}^{(1)}(\omega)}{E_{\mathbf{k}}^e - E_{\mathbf{q}}^e + \hbar\omega + i\eta} + \frac{\mathbf{J}_{e\mathbf{k}-\mathbf{q}}^{\mathrm{THz}} \cdot F_\omega \left[\mathbf{A}(t) \left(f_{e\mathbf{k}}^{(0)}(t) - f_{e\mathbf{q}}^{(0)}(t) \right) \right]}{\left[E_{\mathbf{k}}^e - E_{\mathbf{q}}^e + \hbar\omega + i\eta \right] \left[E_{\mathbf{k}}^e - E_{\mathbf{q}}^e + i\eta \right]} \right\}$$
$$- \frac{1}{L^3} \sum_{\mathbf{q}} N_i^{\mathrm{tot}} \left(L^3 V_{|\mathbf{k}-\mathbf{q}|}^{ei} \right)^3 \left\{ \frac{f_{e\mathbf{q}}^{(1)}(\omega) - f_{e\mathbf{k}}^{(1)}(\omega)}{E_{\mathbf{q}}^e - E_{\mathbf{k}}^e + \hbar\omega + i\eta} + \frac{\mathbf{J}_{e\mathbf{q}-\mathbf{k}}^{\mathrm{THz}} \cdot F_\omega \left[\mathbf{A}(t) \left(f_{e\mathbf{q}}^{(0)}(t) - f_{e\mathbf{k}}^{(0)}(t) \right) \right]}{\left[E_{\mathbf{q}}^e - E_{\mathbf{k}}^e + \hbar\omega + i\eta \right] \left[E_{\mathbf{q}}^e - E_{\mathbf{k}}^e + i\eta \right]} \right\}. \tag{16}$$

Here, the second line equals the right-hand side of the first line if one interchanges $\mathbf{k} \leftrightarrow \mathbf{q}$. Mathematically, this equation is an inhomogeneous Fredholm (integral) equation of the second kind, which can be solved by the Nyström method [10]. The inhomogeneity results from the zeroth-order electron-ion correlation. If $f_{e\mathbf{k}}^{(1)}(\mathbf{A}_i)$ is a solution for the field $\mathbf{A}_i$, then $\sum_i f_{e\mathbf{k}}^{(1)}(\mathbf{A_i})$ is a solution for the field $\sum_i \mathbf{A}_i$, which is the justification for the δ-pulse analysis we use in Sec. IV. The symmetry of Eq. (16) can be seen easily, once we calculate the electron THz current

$$\frac{1}{L^3} \sum_{\mathbf{k}} \mathbf{J}_{e\mathbf{k}}^{\mathrm{THz}} f_{e\mathbf{k}}^{(1)}(\omega) = \frac{1}{L^6} \sum_{\mathbf{k},\mathbf{q}} \frac{\mathbf{J}_{e\mathbf{k}-\mathbf{q}}^{\mathrm{THz}} \left(L^3 V_{|\mathbf{k}-\mathbf{q}|}^{ei} \right)^2}{\hbar\omega + i\Gamma}$$
$$\times \left\{ \frac{f_{e\mathbf{k}}^{(1)}(\omega) - f_{e\mathbf{q}}^{(1)}(\omega)}{E_{\mathbf{k}}^e - E_{\mathbf{q}}^e + \hbar\omega + i\eta} + \frac{\mathbf{J}_{e\mathbf{q}-\mathbf{k}}^{\mathrm{THz}} \cdot F_\omega \left[\mathbf{A}(t) \left(f_{e\mathbf{q}}^{(0)}(t) - f_{e\mathbf{k}}^{(0)}(t) \right) \right]}{\left[E_{\mathbf{q}}^e - E_{\mathbf{k}}^e + \hbar\omega + i\eta \right] \left[E_{\mathbf{q}}^e - E_{\mathbf{k}}^e + i\eta \right]} \right\}, \tag{17}$$

where both contributions are merged in one line. In our numerical analysis, we use this equation for convergence tests. Once we know the current, we can calculate the linear

susceptibility,

$$\chi(\omega) = \frac{J(\omega)}{\epsilon_0 \omega^2 A(\omega)}, \tag{18}$$

and thereby the dielectric function [6],

$$\epsilon(\omega) = \epsilon_0 \left(1 - \frac{\omega_{\mathrm{pl}}^2}{\omega^2} \right) + \frac{J(\omega)}{\epsilon_0 \omega^2 A(\omega)}, \qquad (19)$$

where in both formulas the current and the linear THz polarization point in the same direction. In the following section, we solve these equations numerically, discuss the numerical techniques, and present our results.

IV. NUMERICAL SOLUTION AND RESULTS

Taking advantage of the significant separation of timescales, we simplify the analysis of the full problem by splitting it into three parts: the strong field photoionization with an ultrashort pulse, the subsequent free electron scattering dynamics, and the linear THz spectroscopy, which probes but does not modify the electron relaxation dynamics. The ionization problem is treated by solving the TDSE for a single hydrogen atom:

$$i\hbar \partial_t \Psi(\rho,z;t) = \left[\frac{\mathbf{p}^2}{2m_e} - \frac{e^2}{4\pi\epsilon_0 r} + eE_z(t)z \right] \Psi(\rho,z;t). \qquad (20)$$

We assume that the ionizing electric field is a $\sin^2$-shaped 10-cycle pulse (total duration: 13.33 fs), linearly polarized in z direction, with the center wavelength 400 nm, and a peak intensity of 5×10^{13} W/cm^2. Here, **r** is the electron's space coordinate relative to the nucleus and **p** is the momentum operator, both given in cylindrical coordinates. For a detailed description of the numerical methods used for the solution of the TDSE, we refer to Ref. [11].

To treat the electron Coulomb dynamics, we use a Monte Carlo scheme [4]. Here, the distribution is represented as an ensemble of individual particles whose initial momenta are randomly created using the TDSE-calculated free-electron wavefunctions to generate the initial probability distribution. In the Monte Carlo dynamic evolution, these momenta are changed by random scattering events according to the corresponding scattering probabilities and rates. The resulting histograms extracted from these distributions show stochastic noise in momentum and time. We reduce this noise by averaging 10 runs with 10^7 particles and remove the residual noise with a low-pass filter. More calculational details can be found in the Appendix, where we also give further information on our GPU implementation of the Monte Carlo code.

Equation (16) is solved on a discrete spherical momentum grid (variables $k = |\mathbf{k}|, \theta, \phi$). For the broadenings, we use $\Gamma = 5$ meV and $\eta = 20$ meV. Due to the fact that the zeroth-order distributions are ϕ-angle independent, the ϕ integration can always be evaluated analytically. Here, we calculate $f_{e\mathbf{k}}^{(1)}(\omega)/\cos(\phi_k)$ instead of $f_{e\mathbf{k}}^{(1)}(\omega)$, which is used for the z-polarized probe fields. In both cases, it can be analytically shown that the result is independent of the angle ϕ. The biggest challenge in solving the Fredholm integral Eq. (16) results from the very large differences between the energy expression in the denominators. The electronic energies are in the range of few election volts ($E_{\mathbf{k}}^e \simeq 38.0\,k^2$ meV for k in [1/nm]), but the energy $\hbar\omega$ ($\hbar\omega_{\mathrm{pl}}^e \simeq 17.0$ meV) and the broadening η is only several millielectron volts, which requires an extremely

fine k grid. In our numerical implementation, we resolve the zeroth-order electron density with 150 k- and 128 θ-points, which are equidistantly distributed. However, in order to obtain numerical convergence and stability in the solution of Eq. (16), we would need approximately 2000 k points. Since the full numerical solution on such fine grid would increase the numerical effort by at least two orders of magnitude, we solve the integral equation on the original coarse grid and use a quintic Hermite interpolation inside the integral. The corresponding matrix in the Nyström approximation is still larger than 5 GB, which makes a direct matrix inversion very inefficient. Therefore, we apply the iterative GMRES algorithm [12,13].

The anisotropic distribution of the free electrons directly after the ionization is shown in Fig. 1(a). Whereas we have full rotational symmetry around the polarization axis, strongly anisotropic signatures show up as prominent peaks in the k_z-k_ρ plane. Calculating θ-angle averaged distributions, the initial density features several orders of multiphoton ionization, which are separated by one photon energy as can be seen, e.g., by the black curve in Fig. 1(e). In the subsequent dynamic evolution, these features are smeared out and the anisotropy is reduced due to electron-electron and electron-ion scattering. After 400 fs the distribution is almost isotropic and hardly distinguishable from the final Fermi-Dirac equilibrium distribution.

As an experimentally viable test of the anisotropy, we compute the linear THz probe response assuming a Gaussian THz pulse $\mathbf{A}(t)$ with 50 fs FWHM. We choose z and x polarization here, but the result for an arbitrary polarization direction perpendicular to the z axis would be identical due to the symmetry of the distribution. The THz pulse is delayed relative to the time of the initial distribution $t = 0$ ps, which is the time when the ionizing pulse is completely gone and the free particle distribution of the TDSE calculation becomes static. We center the THz pulse at 0.1 ps, 0.2 ps, and 0.4 ps, where the snapshots of Fig. 1 are taken omitting the 0.0 ps results to avoid an overlap with the ionizing pulse. Figure 2 shows the absolute value of J_e^{pond} and J_e^{THz} for different frequencies ω. The pondermotive current does not change since, for the chosen delays, the total density is constant during the THz probing, whereas the linear THz current reflects the anisotropy of the underlying momentum distributions. This current is, e.g., responsible for the broadening Γ_{Drude} in a simplified Drude treatment of the plasma contributions on the dielectric function:

$$\epsilon(\omega) = \epsilon_0 \left(1 - \frac{\omega_e^{\mathrm{pl}2}}{\omega(\omega + i\Gamma_{\mathrm{Drude}})} \right).$$

To obtain more insights into the THz response directly after the ionization, we replace the 50-fs THz pulse by an ultrashort pulse. Examples of the results are shown in Fig. 3, where we plot the inverse dielectric function Eq. (19). We note the typical resonance near the plasma frequency in the imaginary part features, whereas the real part shows the characteristic dispersive shape. The changes for x-polarized THz probe fields are less pronounced than the ones for the z-polarized case. Here, we even observe THz gain directly after the ionization instead of the usual THz absorption. This implies a light-field-induced
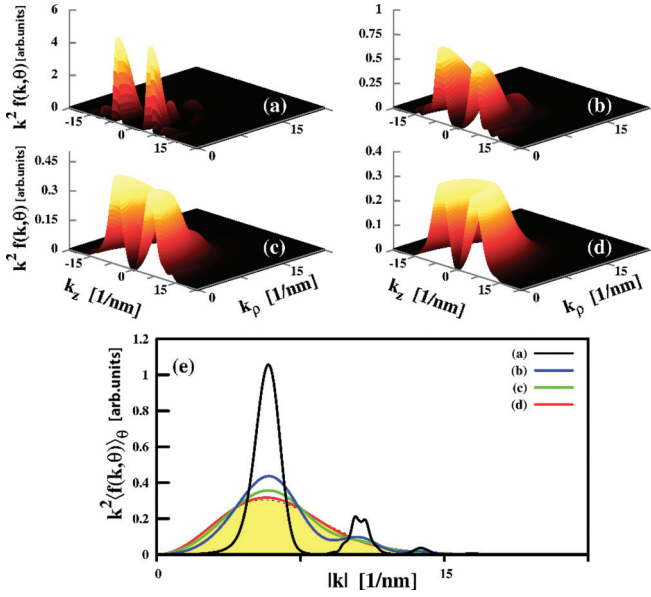
FIG. 1. (Color online) Relaxation of an anisotropic nonequilibrium electron distribution created by ionizing hydrogen atoms with a 400-nm 10-cycle pulse of intensity $I = 5 \times 10^{13}$ W/cm^2. Top: $k^2 f(k,\theta)$ for different times (a) $t = 0.0$ ps, (b) $t = 0.1$ ps, (c) $t = 0.2$ ps, (d) $t = 0.4$ ps. Bottom: in (e) the angle averaged distribution $k^2 \langle f(k,\theta) \rangle_\theta = (k^2/2) \int_0^\pi f(k,\theta) \sin(\theta) d\theta$ for the same times. The shaded area shows the final Fermi Dirac distribution with temperature $T = 13\,878$ K corresponding to an average energy of $\bar{E} = 1.794$ eV. The total electron density is $N_e^{\text{tot}} = 2.086 \times 10^{23}$/m^3 yielding the inverse 3D plasma frequency of approximately $1/f_{\text{pl}}(N_e) = 0.244$ ps.
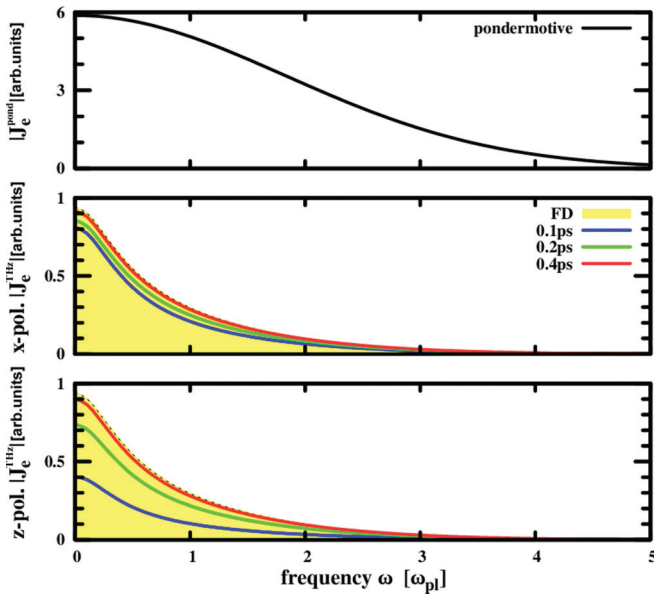

FIG. 2. (Color online) Absolute value of the current $|J| = \sqrt{re[J]^2 + im[J]^2}$, which is induced by the THz probe field $A(\omega)$. Here, we assume an either x- or z-polarized Gaussian pulse with a FWHM of 50 fs and a delay of 0.1 ps, 0.2 ps, and 0.4 ps, relative to the time of the initial TDSE distribution. As a consequence of the carrier anisotropy, the current is also anisotropic for short times and becomes fully isotropic for longer delay times due to the Coulombic scattering events. The characteristic time scale is determined by the inverse plasma frequency.
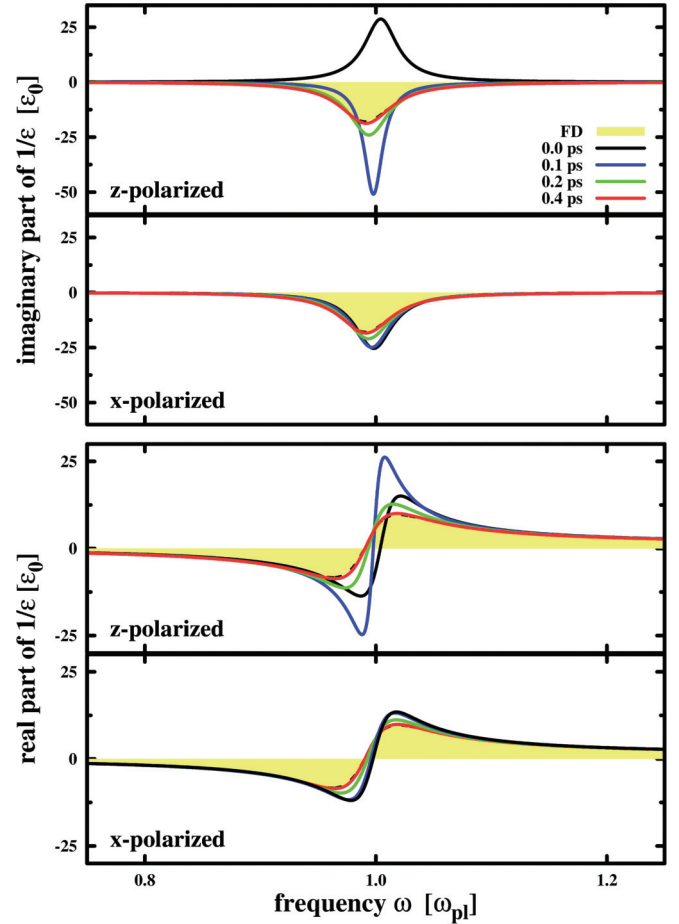

FIG. 3. (Color online) Inverse dielectric function for pulse delays of 0.0 ps, 0.1 ps, 0.2 ps, and 0.4 ps, relative to the time of the initial TDSE distribution. The **A** field is an either x-polarized or z-polarized pulse. The final isotropic Fermi-Dirac distribution is shown as reference (shaded area).

transient population inversion between the THz-coupled angular momentum eigenstates of the hydrogen system.

V. SUMMARY

In this paper, we present a microscopic model to describe the complex dynamics observable in a THz probe experiment of the momentum anisotropy of ultrashort-pulse ionized electron-ion systems. For the model case of hydrogen, we show that this anisotropy influences the electronic properties of the system. Our initial distribution produces THz gain for z-polarized THz probe fields, whereas all other cases have a purely absorptive behavior. It will be interesting to see to which degree the early-time anisotropic plasma relaxation manifests itself also in the optical response and influences the pulse propagation and filamentation dynamics. These features are subjects of ongoing studies.

ACKNOWLEDGMENTS

APPENDIX: GPU CALCULATION

To solve the high-dimensional integrodifferential Eq. (7), we employ the Monte Carlo method implemented on a general purpose graphics processing unit (GPU). A GPU is essentially an accelerated coprocessor, attached to a host computer, on which certain compute intensive functions may be efficiently executed. In comparison to traditional CPUs, which may have 4, 8, or 12 processing cores, typical GPUs consists of hundreds (or potentially thousands) of processor cores that operate in parallel, executing single instruction on multiple data (SIDM architecture). In addition, a GPU contains its own onboard memory, which is roughly 10 times faster than the main memory of standard personal computers. The highly data-parallel and memory bandwidth intensive nature of the Monte Carlo method makes it an excellent candidate for GPU performance scaling. For the comparison between our CPU and GPU implementation, we compare an 8 core workstation (dual processor Intel Xeon X5677 Quad core 3.75 GHz) with an nVidia GTX 480 GPU. In this comparison, we achieve a threefold speedup in our algorithm executing on the GPU compared to an equivalent OpenMP implementation executing in parallel on all 8 cores of the workstation.

An essential requirement for effective Monte Carlo GPU calculations is that one can deal with single-particle scattering events (Fig. 4), which is given by standard Monte Carlo algorithm even for two-particle Coulomb scattering [14,15], which we solve with the self-scattering technique [16]. Due to the large mass difference, the electron-ion scattering rates depend only on the total ion density, which effectively decouples the electron from the ion dynamics. For the electron-electron scattering, an individual particle scatters with another particle taken out of the reference electron distribution. At the scattering time, the scattering mechanism (electron-electron, electron-ion, self-scattering), the particle's new momentum, and time of the next scattering event is randomly calculated according to the corresponding probabilities. However, the reference ensemble remains unchanged and is only updated with the current particle momenta after a dt timestep. Therefore, we have two different times, the particle's individual scattering time, i.e., the point in time when the particle will be scattering next, and the synchronization time, i.e., the time at which the reference particle distributions are updated. Within
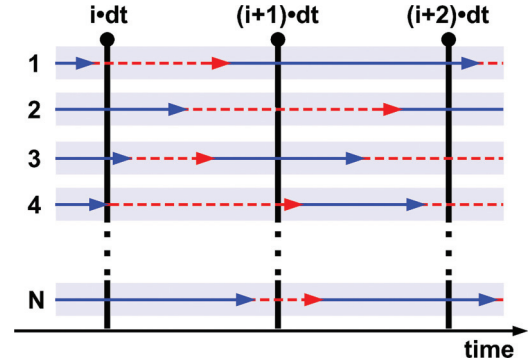

FIG. 4. (Color online) Monte Carlo scattering of N particles. The arrow ends indicate scattering events. The scattering rates and times as well as the particle's final momentum after the scattering are calculated with the current reference distribution from the last synchronization (indicated as vertical lines), which takes place after all scatterings within a dt timestep are done. Generally, a particle can have zero, one, or even many scattering events between two adjacent synchronization points.

a timestep, an electron can have none, one, or even many scatterings, but the timestep must be sufficiently small so that the reference distribution changes only slightly in comparison to the previous one.

In our implementation, we launch 10^7 independent threads of execution, each of which is responsible for one particle's scattering dynamics. These 10^7 threads are automatically multiplexed onto the 480 processing cores available in the GPU by a dedicated hardware scheduler in the GPU. Each thread manages its own linear congruential random number generator based on Marsaglia's Xorshift Random Number Generator as described in Numerical Recipes in C++ [10]. A thread uses its random number generator many times during a scattering event. After a fixed number of timesteps, the reference distribution is copied back to the CPU memory to evaluate the histograms. Afterwards, the GPU calculation starts again.

The limiting bottleneck of our algorithm is that all threads must perform a global synchronization after every timestep. This synchronization must be complete before a thread can retrieve the stored state of its next scattering partner from global memory at the beginning of each simulation timestep. However, not every particle has a scattering event during every single timestep; there are many self-scatterings, i.e., a virtual scattering, where the particle momentum is unchanged, and the calculation time of different scattering events is not equal. But even with these restrictions, we still gain a significant speedup in comparison to a single- or many-core CPU calculations.

[1] T. Popmintchev *et al.*, Science **336**, 1287 (2012).

[2] Y. Huismans *et al.*, Science **331**, 61 (2011).

[3] M. Wickenhauser, X. M. Tong, D. G. Arbo, J. Burgdorfer, and C. D. Lin, Phys. Rev. A **74**, 041402(R) (2006).

[4] B. Pasenow, J. V. Moloney, S. W. Koch, S. H. Chen, A. Becker, and A. Jaron-Becker, Opt. Express **20**, 2310 (2012).

[5] R. Huber, F. Tauser, A. Brodschelm, M. Bichler, G. Abstreiter, and A. Leitenstorfer, Nature (London) **414**, 286 (2001).

[6] D. Golde, M. Kira, and S. W. Koch, Proc. SPIE **6892**, 68921F (2008).

[7] C. Cohen-Tannoudji, J. Dupont-Roc, and G. Grynberg, *Photons and Atoms: Introduction to Quantum Electrodynamics*, 3rd ed. (Wiley, New York, 1989).

[8] See, e.g. Chap. 8 in H. Haug and S. W. Koch, *Quantum Theory of the Optical and Electronic Properties of Semiconductors*, 5th ed. (World Scientific Publishers, Singapore, 2009).

[9] M. Kira, and S. W. Koch, Prog. Quantum Electron. **30**, 155 (2006).

[10] W. H. Press, S. A. Teukolsky, W. T. Vetterling, and B. P. Flannery, *Numerical Recipes: The Art of Scientific Computing*, 3rd ed. (Cambridge University Press, Cambridge, 2007).

[11] S. H. Chen, X. Gao, J. Li, A. Becker, and A. Jaroń-Becker, Phys. Rev. A **86**, 013410 (2012).

[12] R. Barrett *et al.*, *Templates for the Solution of Linear Systems: Building Blocks for Iterative Methods* (SIAM, Philadelphia, 1994).

[13] The implementation of the C++ code for the iterative method was geared to the examples of the *Seldon C++ library for linear algebra*, http://seldon.sourceforge.net/.

[14] C. Jacoboni and P. Lugli, *The Monte Carlo Method for Semiconductor Device Simulation* (Springer, Wien/New York, 1989).

[15] D. Vasileska, S. M. Goodnick, and G. Klimeck, *Computational Electronics: Semiclassical and Quantum Device Modeling and Simulation*, 1st ed. (CRC Press, Boca Raton, 2010).

[16] R. Brunetti, C. Jacoboni, A. Matulionis, and V. Dienys, Physica B **134**, 369 (1985).